Systematic investigation of the benchtop surface wrinkling process by corona discharge

ARTICLE *in* RSC ADVANCES · NOVEMBER 2014

Impact Factor: 3.84 · DOI: 10.1039/C4RA10732B

3 AUTHORS, INCLUDING:

Kang Wei

Alcon

17 PUBLICATIONS **42** CITATIONS

SEE PROFILE

Yi Zhao

The Ohio State University

95 PUBLICATIONS **491** CITATIONS

SEE PROFILE

RSC Advances

PAPER

View Article Online
View Journal | View Issue

Cite this: *RSC Adv.*, 2014, **4**, 59122

Systematic investigation of the benchtop surface wrinkling process by corona discharge†

Kang Wei, Matthew Stevens Rudy and Yi Zhao*

Periodic micro/nanostructures with the characteristic dimensions at single or two length scales have manifested their strengths in providing contact cues to regulate cell alignment and motility, creating diffractive gratings for wavelength selection and pulse compression, and producing tailored surface wettability and adhesion. The currently used lithographic and surface wrinkling methods often require substantial use of special fabrication facilities and a cleanroom environment, and are accompanied by complicated fabrication processes. This paper systematically examines a facile benchtop wrinkling process to produce periodic micro/nanostructures and hierarchical topographies on elastomeric substrates in a general wet laboratory. Atmospheric electric discharge generated by a hand-held corona surface treater produces a rigid thin film atop an elastomeric foundation containing an initial tensile strain. Periodic sinusoidal wrinkled deformations with tailored wavelengths and amplitudes form spontaneously upon stress removal. This process is compatible with commercial tensile test machines and can create elastomeric micro/nanowrinkled structures within minutes. It can also be coupled with softlithography and/or photolithography to generate hierarchical wrinkled topographies with various degrees of anisotropy. This work provides a technical basis for versatile manufacturing of periodic and hierarchical wrinkled topographies at different length scales for various applications.

Received 18th September 2014
Accepted 31st October 2014

DOI: 10.1039/c4ra10732b

www.rsc.org/advances

1. Introduction

Periodically grooved surfaces with characteristic dimensions at the nanoscale, microscale or multiple length scales have sparked immense research interests due to their paramount roles in cell contact guidance,[1–3] optical manipulation[4,5] and surface wettability control.[6,7] In tissue engineering, anisotropic microgrooves/ridges have demonstrated their strengths in reorganizing cytoskeletons and therefore orienting adherent cells,[8] manipulating gene expressions of aligned cells,[9] and regulating cell proliferation, migration, and differentiation.[10] Similarly, anisotropic nanogrooves/ridges influence cell morphology and motility,[11] and regulate focal adhesion and cell orientation.[12,13] Hierarchical surface topographies with superimposed micro/nanogrooves have been used to investigate the respective effects of microstructures and nanostructures as well as their synergic effects on cells.[14,15] In optical manipulation, subwavelength sawtooth, sinusoidal or rectangular grooves (blazed, holographic or laminar gratings) have found applications in laser excitation, analytical spectroscopy, wave division multiplexing, and other diffractive imaging systems.[16] In surface science, submicrometer or hierarchical grooves have displayed anisotropic wetting behaviours from superhydrophobic to superhydrophillic ranges, which precipitated the exploration of open-channel microfluidics.[17–19] Despite these exciting discoveries, fabrication efforts for creating such periodic and hierarchical micro/nanostructures are not trivial. In above studies, micro/nanostructures are often created on a rigid substrate by lithographic processes and can be later transferred to soft substrates.[20] Particularly, microscale topographies can be fabricated by photolithography,[21] reactive ion etching,[22] or laser interference lithography[5] that requires cleanroom environment and facilities, or by hot embossing[23] that relies on pre-machined molds. Nanoscale topographies can be created by direct writing using focused ion beam,[24] electron beam,[25] or nanoimprint lithography[26] through costly and time-consuming processes. Notably, fabrication of hierarchical structures whose characteristic dimensions are at multiple length scales is even more arduous due to the increased structural complexity.

Surface wrinkling emerges as a promising method for producing grooved micro/nanostructures on soft substrates.[27,28] This method leverages mechanical buckling occurring during the compression relief of a pre-strained bi-layered substrate that is comprised of a rigid thin film adhered to a soft elastomeric foundation.[29] It is well established that with a small pre-strain ($\varepsilon \leq 5\%$), the wavelength (λ) of surface wrinkles can be predicated by energy minimization analysis:[30,31]

Laboratory for Biomedical Microsystems, Department of Biomedical Engineering, The Ohio State University, Columbus, OH, 43210 USA. E-mail: zhao.178@osu.edu

† Electronic supplementary information (ESI) available: Characterization of water contact angles on nanowrinkled and microwrinkled surfaces in directions parallel and orthogonal to the sinusoidal groove. See DOI: 10.1039/c4ra10732b

$$\lambda = 2\pi t_f \left[\frac{E_f\left(1-\upsilon_s{}^2\right)}{3E_s\left(1-\upsilon_f{}^2\right)}\right]^{1/3} \quad (1)$$

where t denotes the thickness, E denotes the Young's modulus, and υ denotes the Poisson's ratio; the subscripts s and f refers to the soft elastomeric substrate and the rigid thin film, respectively. When a large pre-strain ($\varepsilon \geq 5\%$) is applied, nonlinear deformation occurs. The wavelength (λ') is modified as:[30,31]

$$\lambda' = \frac{\lambda}{(1+\varepsilon)\left[1+\frac{5}{32}(1+\varepsilon)\right]^{1/3}} \quad (2)$$

It is seen from eqn (2) that the geometries of wrinkled topographies can be tuned by changing the thickness of the rigid thin film, the stiffness difference between the rigid thin film and the underlying elastomeric substrate, and/or the magnitude of the applied pre-strain.

In surface wrinkling, spontaneous formation of continuous sinusoidal topographies upon stress removal eliminates the use of photomasks or pre-machined molds in lithographic methods. Nonetheless, special fabrication equipment is still required to produce the stiffness mismatch between the rigid thin film and the elastomeric substrate. Such stiffness mismatch is introduced by either depositing an additional rigid thin film on top of a pre-strained elastomeric substrate by spin-coating, sputtering or electron beam evaporation,[32–35] or by oxidizing the top surface of the elastomeric substrate using plasma,[36,37] ion beams,[38] or a UV source.[39,40] The use of plasma or ion beams necessitates an enclosed chamber with a precisely controlled vacuum pressure and special gas atmosphere.[32–38] The pumping and purging sequences inevitably elongate the fabrication process although the deposition/oxidation process itself may take only a fairly short period of time.[37,41] Moreover, the chamber for deposition/oxidation is often housed in a cleanroom environment due to the stringent requirement of air and particle control, which increases the fabrication cost and somewhat affects the accessibility for users. Although UV ozonolysis eliminates the need of cleanroom access and vacuum supply, the surface oxidation is rather slow, *i.e.* about 10 to 60 min exposure of UV to create wrinkles with the wavelengths from few to hundreds of μm.[40] In addition, most commercial tensile machines cannot be accommodated within the deposition/oxidation chamber due to their bulky sizes and possible malfunctions by high energy sources. Custom-built stretching apparatuses are used to stretch the elastomeric substrates and hold them at a designated pre-strain, which are later transferred into the deposition/oxidation chamber. These custom-built apparatuses often lack precise control of the pre-strain and the un-loading rate, and may cause inconsistent surface topographies and unexpected surface defects.[42]

Recently, a few studies reported a promising technology using corona-discharge as an auxiliary means to create and expand an elastic crust on the surface of UV-cured polymer, facilitate microwrinkle-to-fold transition, and form isotropic hierarchical folds.[43,44] The potential of using solely coronadischarge to engineer anisotropic surface topographies of different length scales, however, draws limited attention given deficient quantitative studies on coronadischarge induced surface wrinkling. In an effort to encourage its wide-spread use, we systematically investigate the capability of coronadischarge for creating both periodic and hierarchical wrinkled structures with controlled dimensions. The process can be carried out within a general wet laboratory environment and is compatible with commercial tensile test equipment. Sinusoidal wrinkled topographies with the wavelength ranging from about 500 nm to 3000 nm were created on the polydimethylsiloxane (PDMS) surface within minutes. Hierarchical wrinkled topographies with parallel or orthogonal alignment patterns were also created by coupling this method with soft-lithography and/or photolithography. This study paves the way for wide-spread adoption of coronadischarge based benchtop surface wrinkling given its little reliance on expensive deposition/oxidation equipment and/or cleanroom environment, user-friendliness, and versatility to manufacture wrinkled topographies of different length scales.

2. Experimental

2.1. Elastomeric membrane preparation

PDMS (Sylgard 184, Dow Corning, MI) was prepared by mixing the base prepolymer and the curing agent at a weight ratio of 10 : 1. The prepolymer was degassed in vacuum for 30 min, poured into a Petri-dish, and allowed to spread into a layer with a thickness of 2 mm. After cross-linking the mixture was baked on a hotplate at 65 °C for 2 h. The PDMS substrate was cut into rectangular elastomeric membranes with 55 mm in length and 10 mm in width. The membranes were cleansed by 70% ethanol before use.

2.2. Corona discharge induced surface wrinkling

The benchtop surface wrinkling process is depicted in Fig. 1a. Briefly, the rectangular PDMS membrane was mounted on a commercial tensile test apparatus (100Q250-6, Testresources, Shakopee, MN) and stretched lengthwise at a loading rate of 100 μm s^{-1}. While the PDMS membrane was held at a given pre-strain, it was approached to the discharge tip of a hand-held high frequency corona surface treater (BD-20AC, Electro-technic Products, Chicago, IL) and was kept at a tip-to-surface distance of 5 mm. As shown in Fig. 1b, the discharge tip was connected to the output A of the corona tester, while the output B was grounded. The power transformer T1 set up a high voltage which caused a spark gap to break down at the rate twice of the line frequency (100–120 Hz). The spark gap charged the capacitors C1 and C2 that were connected to the primary windings of the resonator coil T2 with an air core. Because of the inductance of primary windings of T2 and capacitors, an oscillating current with high frequency was set up in the circuit. The spark gap was adjusted to reach the resonant frequency of the circuit about 3.8 MHz. High voltage was thus induced in the secondary windings of T2, causing the corona discharge at the output A (Fig. 1c and d). In this study, the operational power of

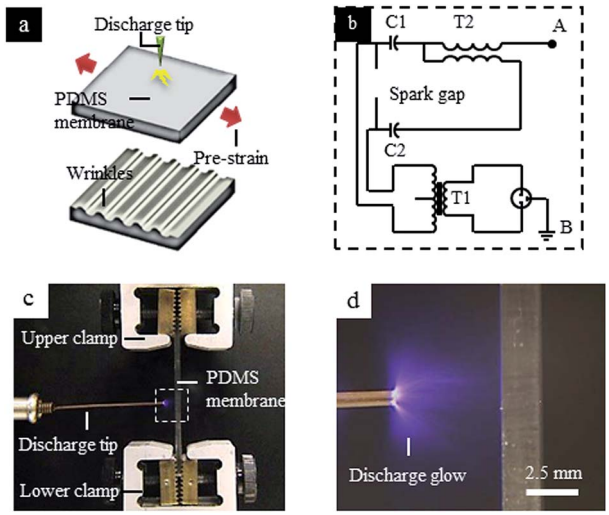

Fig. 1 Benchtop wrinkling process: (a) schematic representation of corona discharge induced surface wrinkling; (b) the electrical diagram for corona discharge generation; (c) the experimental setup (the discharge is connected to output A in (b)); (d) magnified view of the highlighted regions in (c), showing bluish glow due to partial electrical breakdown of the air near the discharge tip.

the corona surface treater was measured by a power monitor (P4460 Kill A Watt® EZ, P3 International, NY) and was kept as 27 W throughout all experiments.

After certain discharge time, the substrate was released to the original length at an un-loading rate of 100 μm s^{-1}. The entire process was carried out at room temperature. In order to determine the dependence of the wrinkle wavelength on the key operational parameters in the benchtop wrinkling process, a parametric study was performed by varying the pre-strain from 5% to 40% and the discharged time from 0.5 min to 8 min.

2.3. Creating bi-layered wrinkled topographies

Hierarchical wrinkled topographies were created by combining benchtop surface wrinkling with soft lithography (Fig. 2a). The as-wrinkled PDMS substrate that underwent the prestrain of 20% and the discharge time of 4 min was soaked in 0.5% (hydroxypropyl)methyl cellulose (Sigma-Aldrich, MO) for 10 min, rinsed with de-ionized water, and air-dried. Degassed PDMS prepolymer was poured on top of the as-wrinkled PDMS membrane, allowed to spread into a layer with the thickness of 2 mm, and cured on a hot plate at 65 °C for 2 h. The replicated substrate with the surface topographies complementary to those on the master PDMS substrate was then peeled off. Afterwards, the replica substrate was stretched at 0° or 45° to the longitudinal axis of the existing wrinkles and was subject to the benchtop wrinkling process with the pre-strain of 20% and the discharge time of 1 min.

2.4. Creating wrinkled topographies on microfabricated structures

Hierarchical surface topographies were also created by combining the benchtop wrinkling process with lithographic

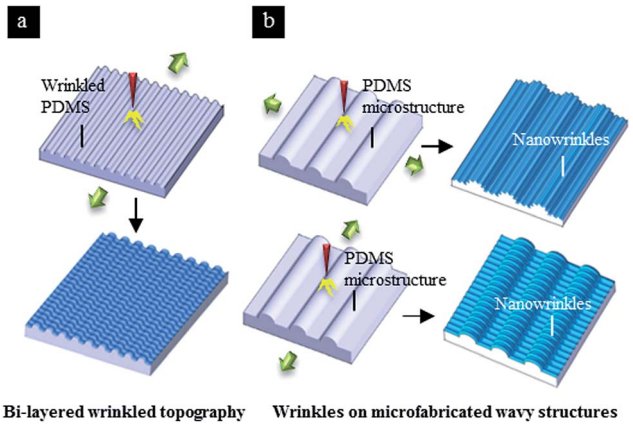

Fig. 2 Fabrication processes for creating bi-layered wrinkled topographies: (a) the process of creating bi-layered wrinkled topography by overlaying a layer of additional wrinkles on an existing layer of replicated wrinkles; and (b) the process of creating continuous wrinkles on microfabricated wavy structures.

approaches (Fig. 2b). To demonstrate this, nanowrinkles were superimposed on microfabricated structures with a wavy surface. A silicon wafer was vapor primed with Hexamethyldisilazane (HMDS) and spin-coated with AZ9260 photoresist (AZ Electronic Materials, NJ) at 2400 rpm for 60 s. The wafer was soft-baked at 110 °C for 80 s, exposed to 365 nm UV at 20 mW cm^{-2} for 75 s, and developed in AZ 400K (Microchem Corporation, MA) for 3 min. The wafer was then placed on a hotplate at 110 °C for 120 s to allow the AZ resist to reflow, forming an array of microstructures with continuous thickness change. The wavy pattern was then transferred to a PDMS substrate by replica molding twice. Afterwards, the PDMS substrate was stretched uni-axially at a degree of 0° or 90° to the longitudinal direction of the wavy microstructures and was subject to the benchtop wrinkling process with the pre-strain of 40% and the discharge time of 30 s.

2.5. Characterization of surface topographies

Atomic force microscopy (Bruker Nanoscope III Multimode SPM, Bruker Biosciences Corporation, MA) was used to examine the surface profiles of the wrinkled structures on various substrates. The wavelength of the wrinkles in each sample was determined by optical microscopy (Nikon Eclipse LV 100, 100× objective) at eight different locations in the center regions of the discharge area (100 × 100 μm^2). Scanning electron microscopy (SEM, Hitachi S-3000H, UK) was used to examine the wavy PDMS microstructures replicated from the reflowed AZ photoresist.

3. Results and discussion

3.1. Wrinkle geometries changes with the operational parameters

During the benchtop wrinkling process, the high electric field in the gap between the tip electrode and the substrate caused partial electric breakdown that ionized the air surrounding the

electrode and created a plasma zone containing reactive oxygen species. It converted the Si–CH_3 bonds at the outermost surface of the PDMS into polar functional groups (mainly, Si–OH), leaving a strain-free silica-like skin atop the prestrained substrate. Upon unloading, the substrate contracted back to its strain-free configuration at the expense of surface undulations to minimize the total elastic energy. Results showed that the surface exhibited anisotropic wavy patterns where the longitudinal axis of the sinusoidal groove formed only perpendicular to the direction of the applied pre-strain. Such topographical anisotropy was also evidenced by distinct water contact angles measured parallel and orthogonal to the direction of the wrinkles (Table S1 and Fig. S1†). With the applied operational parameters (pre-strain of 5% to 40% and discharge time of 0.5 min to 8 min), the wrinkle wavelength ranged from about 500 nm to 3000 nm (Fig. 3a). As expected, at a given pre-strain, the wrinkle wavelength increased with the discharge time; while with a given discharge time, the wrinkle wavelength decreased with the increase of the pre-strain. Consequently, a short discharge time with a large magnitude of pre-strain generally led to a small wrinkle wavelength. For instance, wrinkled structures with the average wavelength of about 574 nm were obtained with the pre-strain of 40% and the discharge time of 0.5 min; the wavelength increased to 2.5 μm when the pre-strain decreased to 5% and the discharge time increased to 8 min (Fig. 3b). The amplitude-to-wavelength ratios of these two wrinkled structures were similar: 0.10 for the nanowrinkles whose average amplitude was about 62 nm; and 0.12 for the microwrinkles whose average amplitude was about 295 nm. The amplitude-to-wavelength ratios of samples obtained under other operational parameters were also around 0.10. This indicated that although the thickness of the discharge-induced oxide layer changed the wavelength and the amplitude, the changes were proportional. Such observation agrees well with previous findings in plasma oxidation methods.[45,46]

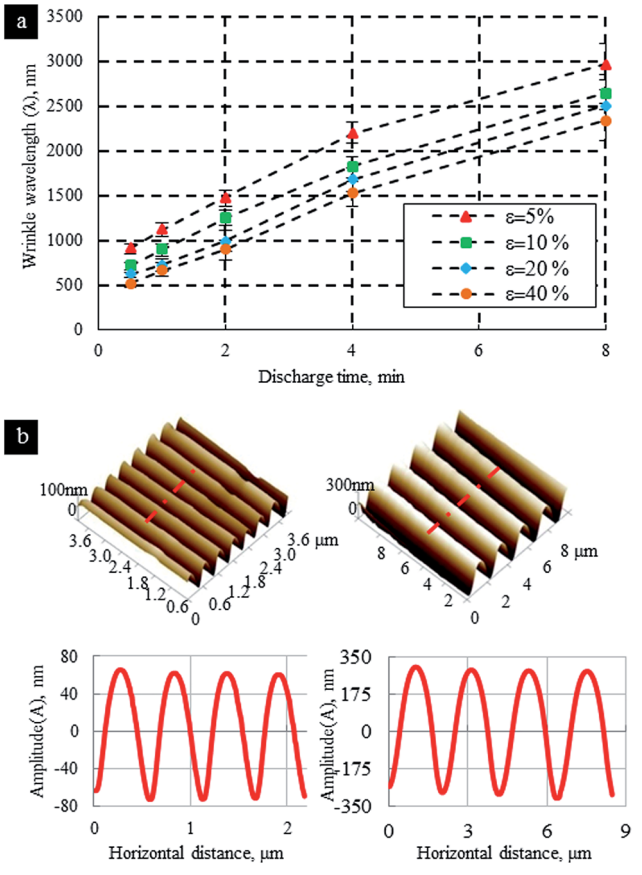

Fig. 3 Characterization of single-layered wrinkles: (a) parametric studies of wrinkle geometries with the pre-strain and the discharge time at the tip-surface distance of 5 mm; and (b) the resulting nanoscale (pre-strain: 40%; discharge time: 0.5 min) and microscale (pre-strain: 5%; discharge time: 8 min) wrinkled structures.

3.2. Bi-layered wrinkled topographies

Benchtop wrinkling process can successfully produce an additional layer of wrinkled structures on the PDMS replica of an existing wrinkle template.[40] When the replicated wrinkles and the additional wrinkles intersect at 90°, the bi-layered superimposed wrinkled topography can be estimated by:

$$z_{a+r} = A_r \sin\left(\frac{2\pi}{\lambda_r}x\right) + A_a \sin\left(\frac{2\pi}{\lambda_a}y\right) \quad (3)$$

where z, A and λ are the height, the amplitude and the wavelength of the wrinkles; the subscripts r and a denote the replicated and the additional wrinkles, respectively; and the subscript a + r denote the superimposed wrinkled structures. Based on the experimental results in single-layered wrinkles, the amplitude-to-wavelength ratio was set as a constant value of 0.10 for both the replicated wrinkles and the additional wrinkles. The profiles of the superimposed wrinkled structures can be obtained analytically (Fig. 4). It is seen that the additional wrinkles cut the wrinkle replica into an alternated array of protrusions and depressions. The protrusions occurred where the crests of the replicated wrinkles and of the additional

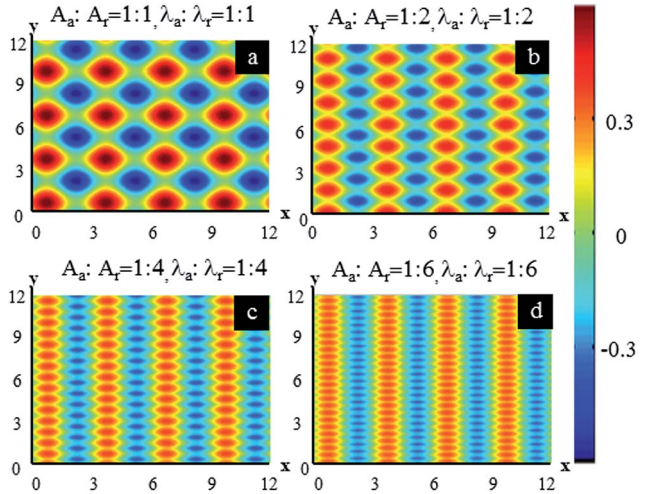

Fig. 4 Dimensionless analytical estimation of superimposed bi-layered wrinkled topographies at different wavelength ratios (λ_r/λ_a). λ_r: dimensionless wavelength of the replicated wrinkles; λ_a: dimensionless wavelength of the additional wrinkles. λ_a = 0.5, 0.75, 1.5 and 3; λ_r = 3.

wrinkles met. Likewise, the depressions occurred where the troughs of the replicated wrinkles and of the additional wrinkles met. The projection areas of the protrusions (or the crests) were diamond-shaped, whose length-to-width ratio increased with the wavelength ratio between the replicated and the additional wrinkles (λ_r/λ_a). A representative pattern of the alternative protrusions/depressions were shown by superimposing the additional wrinkles with the wavelength of 730 nm on top of the replicated wrinkles with the wavelength of 1.6 μm ($\lambda_r/\lambda_a \approx 2.2:1$ at 90°) (Fig. 5a). As the wavelength ratio increased, the additional wrinkles embossed slightly on top of the replicated wrinkles. This can be seen from the bi-layered wrinkled structures with the wavelength ratio $\lambda_r/\lambda_a \approx 4.5$, where the additional (pre-strain: 40%; discharge time: 0.5 min) and replicated wrinkles (pre-strain: 40%; discharge time: 8 min) had respective wavelengths of 510 nm and 2.3 μm (Fig. 5b). The bi-layered wrinkled topographies also varied with the intersection angle. For instance, when the additional wrinkles with the wavelength of 1.6 μm (pre-strain: 20%; discharge time: 4 min) superimposed on top of the replicated wrinkles with the wavelength of 1.8 μm (prestrain: 20%; discharge time: 4 min) at 45°, isolated islands were observed (Fig. 5c).

3.3. Wrinkles on microfabricated wavy structures

Although microstructures with rectangular cross sections are commonly used for demonstrating combined micro/nanostructures,[15,47,48] patterning of continuous nanowrinkled structures on existing microstructures is still challenging.[49,50] This is due to the fact that there is a vast difference of strain magnitude between the top surface of the microstructures and the base substrate. Due to the sharp thickness change, the elastic energy upon pre-straining is mainly stored in the base substrate and at the root area of the microstructures, leading to very small magnitude of strain on the top surface. In this study, a PDMS substrate with an array of wavy microstructures (height: 8 μm; width: 28 μm; pitch: 50 μm) was chosen as the elastic substrate for wrinkle generation (Fig. 6). The wavy geometries ensured that a continuous strain profile upon pre-straining and therefore a continuous wrinkled pattern on the sloped top surface. The results showed that continuous wrinkles occurred in the entire area exposed to the corona discharge, both on the wavy microstructures and on the base substrate. In the samples where the wrinkles were parallel to the wavy microstructures (Fig. 7a and b), the wrinkle wavelength on the wavy microstructures was slightly greater than that on the base substrate. As seen in the figure, there were 13 wrinkles on both the base substrate and the wavy structure. Since the wavy structure had a longer tracing length due to the curved shape, its average wrinkle wavelength was greater. This wavelength difference indicated that the top surface of the wavy structure may experience a slightly lower magnitude of pre-strain than that of the base substrate due to the thickness difference. In the samples where the wrinkles were perpendicular to the wavy microstructures (Fig. 7c and d), no substantial wavelength difference was observed between the top surface of the wavy structures and the base substrate, as evidenced by the line-scanning measurements. This was attributed to the uniform strain field in the entire top surface of the sample upon uni-axial stretching along the longitudinal axis of the wavy structures.

3.4. Wrinkled area and the wavelength uniformity

Different from previous surface wrinkling technologies where the entire top surface was stiffened by placing the samples in an ionized environment, or covered by an additional layer, the corona discharge induced oxidation is a local effect. In particular, the corona discharge ionizes air and produces reactive oxygen species only in the vicinity zone surrounding the discharging tip. In this study, the distance between the discharging tip and the PDMS surface was determined as 5 mm through a trial-and-error experiment. Larger distances substantially increased the time needed for wrinkle formation; while smaller distances led to surface cracking and damage.

The results showed that wrinkles were observed only in a circular region that directly faced the discharging tip. No

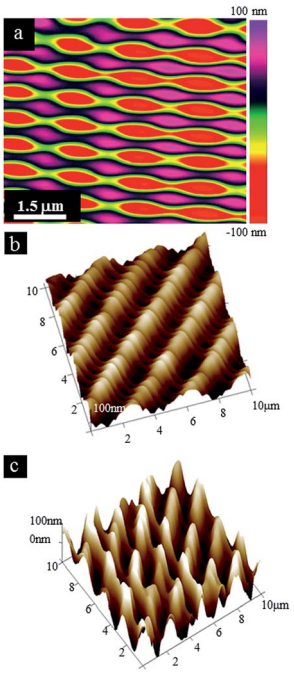

Fig. 5 AFM micrographs of bi-layered wrinkled topographies: (a) $\lambda_r : \lambda_a \approx 2.2 : 1$ at 90° intersection angle; (b) $\lambda_r : \lambda_a \approx 4.5 : 1$ at 90° intersection angle; and (c) $\lambda_r : \lambda_a \approx 1.1 : 1$ at 45° intersection angle.

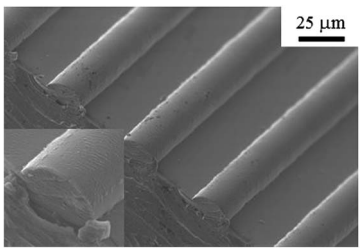

Fig. 6 SEM micrograph of the PDMS substrate with wavy microstructures. The inset gives a magnified view.

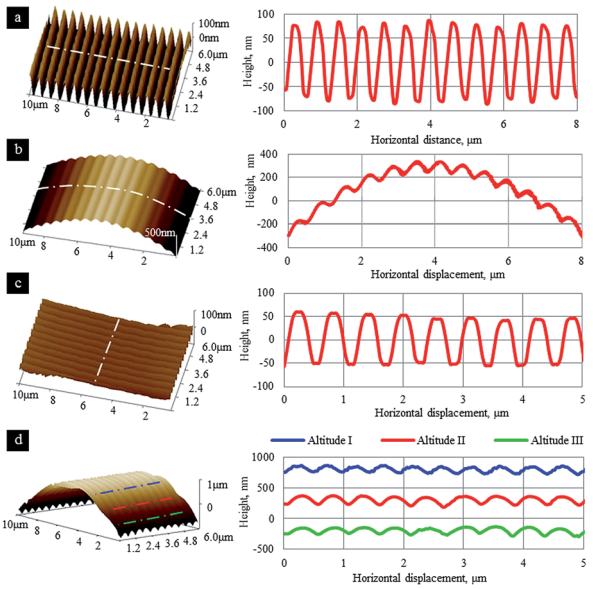

Fig. 7 Geometric characterization of wrinkles on the wavy microstructures. In (a) & (b) nanowrinkles were parallel to the wavy microstructures; and in (c) & (d) nanowrinkles were orthogonal to the wavy microstructures. (a) & (c) showed the wrinkles on the base substrate, while (b) & (d) show the wrinkles on the slope surfaces of the wavy microstructures. The right column shows line-scanning data corresponding to the AFM micrographs on the left.

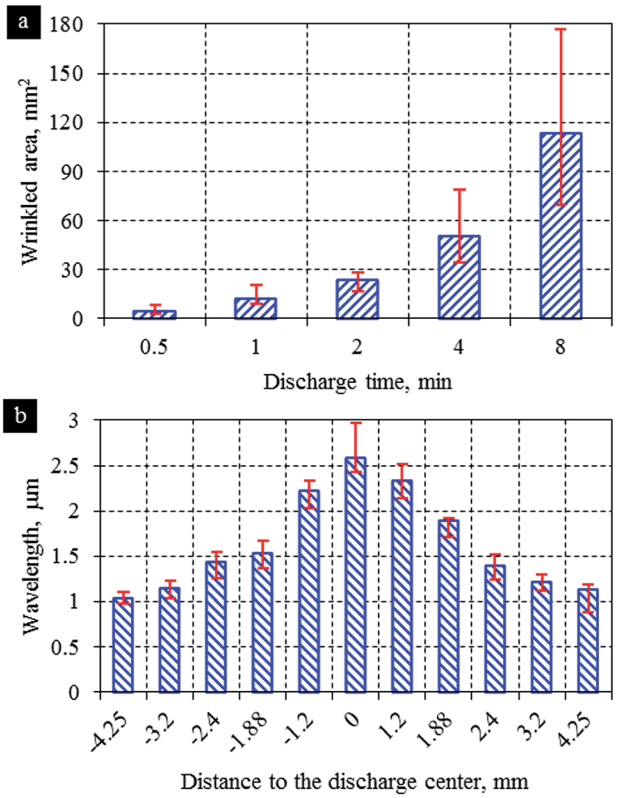

Fig. 8 Characterization of the wrinkled area and wavelength uniformity: (a) the area of region with discernible wrinkled structures with the discharge time of 0.5, 1, 2, 4 and 8 min. The pre-strain is 40% and the tip-surface distance is 5 mm; and (b) the wrinkle wavelength change within the wrinkled area. The pre-strain is 40% and the discharge time is 8 min.

wrinkled structures were discernible beyond the region. With the fixed tip-surface distance of 5 mm, the average area of the region exhibiting discernible wrinkled structures was dependent on the discharging time. With 40% pre-strain, the average area ranged from 4.9 mm^2 at 0.5 min to 113 mm^2 at 8 min (Fig. 8a).

Within the wrinkled region, the wrinkle geometries varied by location. The wrinkle wavelength reached the maximal at the center and gradually reduced as the distance from the center increased. Fig. 8b showed the lengthwise wavelength distribution on a sample with the pre-strain of 40% and the discharge time of 8 min. The wavelength decreased from about 2.59 μm in the discharge center to about 1.1 μm at the distance of 4.25 mm from the center.

The gradient wrinkle wavelength was due to the spatial distribution of reactive oxygen species. Since a point electrode was used to produce corona discharge, the electric field weakened as the distance from the electrode increased, which caused a heterogeneous distribution of reactive species with the highest concentration in the very vicinity of the electrode and the lowest concentration in the outer edge of the corona.[51,52] Such heterogeneous concentration caused thickness variation of the silica thin film, *i.e.* the silica layer at in the center of the discharged region was the thickest and became thinner in the peripheral areas. According to eqn (2), a gradient wrinkle wavelength was expected.

For the samples with the average wrinkle wavelength of 2.59 μm in the discharged center, the wavelength gradient was measured as 0.39 μm mm^{-1}. This gradient is acceptable for applications where the area of interest is fairly small. As an example, for a circular area in the discharged center with 500 μm in diameter, the wavelength change is 0.0975 μm (or 3.76%). For applications where wrinkles with more uniform wavelength are needed in a relatively large area, several possible routes can be performed to improve the wavelength uniformity. First, an array of point electrodes, a wire electrode or a planar electrode can be used to generate a relatively uniform electrical field and thus homogenous concentration of reactive species within the area of interest. It is noted that the planar electrodes with small curvatures generally require a higher electrical field to induce the discharge. The tip-surface distance needs adjustment accordingly. Alternatively, the tip electrode can be mounted on a motorized stage and sweep over the area of interest back and forth while keeping a constant tip-surface distance. The wavelength uniformity can also be enhanced by placing a dielectric mask on top of the sample, which exposes the central area and shields the peripheral area, similar as in other surface wrinkling studies.[53–56] The strategy for enhancing the wavelength uniformity in a larger area is a focus of our future research.

4. Conclusions

A benchtop wrinkling process using corona discharge is systematically examined. Single-layered wrinkled topographies with the wavelength from a couple of hundred nm to several microns were created by discharge induced surface oxidation of pre-strained PDMS substrates. The process can be accomplished in minutes in a general wet laboratory without the need of clean room environment or facilities for deposition or surface coating. Pre-straining can be applied and held by commonly used tensile test apparatus while the surface of interest is subject to discharge. The process can be combined with softlithographic and/or photolithographic processes for creating bilayered wrinkled structures or continuous wrinkled topographies on microfabricated wavy structures. The changes of geometries of the wrinkled structures with the operational parameters and the pre-strain orientations were elaborated. It is recognized that the benchtop surface wrinkling process is limited by the small effective wrinkled area and the poor wavelength uniformity, although it can be improved by changing the electrode geometries, using motorized electrodes, or with the help of a shielding mask.

Acknowledgements

This works is partially funded by a NSF CAREER Award under the number 0954013 and a NSF NUE grant under the number of 1138236. The authors also thank HHMI for Med into Grad program and Pelotonia graduate fellowship for the student support. The authors also thank Dr Jun Liu for her generous facilities support and Dr David Lee for his technical assistance in experiments.

References

1 T. A. Desai, *Med. Eng. Phys.*, 2000, **22**, 595–606.
2 J. Y. Lim and H. J. Donahue, *Tissue Eng.*, 2007, **13**, 1879–1891.
3 E. Martinez, E. Engel, J. Planell and J. Samitier, *Ann. Anat.*, 2009, **191**, 126–135.
4 H. Kikuta, H. Toyota and W. Yu, *Opt. Rev.*, 2003, **10**, 63–73.
5 C. Lu and R. Lipson, *Laser Photonics Rev.*, 2010, **4**, 568–580.
6 A. Marmur, *Langmuir*, 2003, **19**, 8343–8348.
7 D. Quéré, *Annu. Rev. Mater. Res.*, 2008, **38**, 71–99.
8 Y. Zhao, H. Zeng, J. Nam and S. Agarwal, *Biotechnol. Bioeng.*, 2009, **102**, 624–631.
9 M. J. Dalby, M. O. Riehle, S. J. Yarwood, C. D. Wilkinson and A. S. Curtis, *Exp. Cell Res.*, 2003, **284**, 274–282.
10 A. Mata, C. Boehm, A. J. Fleischman, G. Muschler and S. Roy, *Biomed. Microdevices*, 2002, **4**, 267–275.
11 E. K. Yim, R. M. Reano, S. W. Pang, A. F. Yee, C. S. Chen and K. W. Leong, *Biomaterials*, 2005, **26**, 5405–5413.
12 L. Prodanov, J. te Riet, E. Lamers, M. Domanski, R. Luttge, J. J. van Loon, J. A. Jansen and X. F. Walboomers, *Biomaterials*, 2010, **31**, 7758–7765.
13 A. I. Teixeira, G. A. McKie, J. D. Foley, P. J. Bertics, P. F. Nealey and C. J. Murphy, *Biomaterials*, 2006, **27**, 3945–3954.
14 M. T. Eliason, J. L. Charest, B. A. Simmons, A. J. García and W. P. King, *J. Vac. Sci. Technol., B: Microelectron. Nanometer Struct.–Process., Meas., Phenom.*, 2007, **25**, L31–L34.
15 M. J. Lopez-Bosque, E. Tejeda-Montes, M. Cazorla, J. Linacero, Y. Atienza, K. H. Smith, A. Llado, J. Colombelli, E. Engel and A. Mata, *Nanotechnology*, 2013, **24**, 255305.
16 A. Al-Azzawi, *Physical optics: principles and practices*, CRC Press, 2006.
17 W. Li, G. Fang, Y. Li and G. Qiao, *J. Phys. Chem. B*, 2008, **112**, 7234–7243.
18 D. Xia, X. He, Y.-B. Jiang, G. P. Lopez and S. Brueck, *Langmuir*, 2010, **26**, 2700–2706.
19 Y. Zhao, Q. Lu, M. Li and X. Li, *Langmuir*, 2007, **23**, 6212–6217.
20 Y. Xia and G. M. Whitesides, *Annu. Rev. Mater. Sci.*, 1998, **28**, 153–184.
21 M. J. Madou, *Fundamentals of microfabrication: the science of miniaturization*, CRC press, 2002.
22 H. Jansen, H. Gardeniers, M. de Boer, M. Elwenspoek and J. Fluitman, *J. Micromech. Microeng.*, 1996, **6**, 14.
23 M. Heckele and W. Schomburg, *J. Micromech. Microeng.*, 2004, **14**, R1.
24 F. Watt, A. Bettiol, J. Van Kan, E. Teo and M. Breese, *Int. J. Nanosci.*, 2005, **4**, 269–286.
25 A. A. Tseng, K. Chen, C. D. Chen and K. J. Ma, *IEEE Trans. Electron. Packag. Manuf.*, 2003, **26**, 141–149.
26 H. Schift, *J. Vac. Sci. Technol., B: Microelectron. Nanometer Struct.–Process., Meas., Phenom.*, 2008, **26**, 458–480.
27 C.-M. Chen and S. Yang, *Polym. Int.*, 2012, **61**, 1041–1047.
28 S. Yang, K. Khare and P.-C. Lin, *Adv. Funct. Mater.*, 2010, **20**, 2550–2564.
29 Z. Huang, W. Hong and Z. Suo, *Phys. Rev. E: Stat., Nonlinear, Soft Matter Phys.*, 2004, **70**, 030601.
30 H. Jiang, D.-Y. Khang, J. Song, Y. Sun, Y. Huang and J. A. Rogers, *Proc. Natl. Acad. Sci. U. S. A.*, 2007, **104**, 15607–15612.
31 D. Y. Khang, J. A. Rogers and H. H. Lee, *Adv. Funct. Mater.*, 2009, **19**, 1526–1536.
32 J. Y. Chung, T. Q. Chastek, M. J. Fasolka, H. W. Ro and C. M. Stafford, *ACS Nano*, 2009, **3**, 844–852.
33 B. Ned, B. Scott, G. E. Anthony, W. H. John and M. W. George, *Nature*, 1998, **393**, 146–149.
34 H. Vandeparre and P. Damman, *Phys. Rev. Lett.*, 2008, **101**, 124301.
35 J. Yin and C. Lu, *Soft Matter*, 2012, **8**, 6528–6534.
36 N. Bowden, W. T. S. Huck, K. E. Paul and G. M. Whitesides, *Appl. Phys. Lett.*, 1999, **75**, 2557–2559.
37 P. C. Lin and S. Yang, *Appl. Phys. Lett.*, 2007, 90.
38 M.-W. Moon, S. H. Lee, J.-Y. Sun, K. H. Oh, A. Vaziri and J. W. Hutchinson, *Proc. Natl. Acad. Sci. U. S. A.*, 2007, **104**, 1130–1133.
39 K. Efimenko, M. Rackaitis, E. Manias, A. Vaziri, L. Mahadevan and J. Genzer, *Nat. Mater.*, 2005, **4**, 293–297.
40 A. Chiche, C. M. Stafford and J. T. Cabral, *Soft Matter*, 2008, **4**, 2360–2364.

41 X. Jiang, S. Takayama, X. Qian, E. Ostuni, H. Wu, N. Bowden, P. LeDuc, D. E. Ingber and G. M. Whitesides, *Langmuir*, 2002, **18**, 3273–3280.
42 A. Schweikart and A. Fery, *Microchim. Acta*, 2009, **165**, 249–263.
43 P. Kim, M. Abkarian and H. A. Stone, *Nat. Mater.*, 2011, **10**, 952–957.
44 J. B. Kim, P. Kim, N. C. Pégard, S. J. Oh, C. R. Kagan, J. W. Fleischer, H. A. Stone and Y.-L. Loo, *Nat. Photonics*, 2012, **6**, 327–332.
45 F. A. Bayley, J. L. Liao, P. N. Stavrinou, A. Chiche and J. T. Cabral, *Soft Matter*, 2014, **10**, 1155–1166.
46 N. Bowden, W. T. Huck, K. E. Paul and G. M. Whitesides, *Appl. Phys. Lett.*, 1999, **75**, 2557–2559.
47 T. Senn, J. Esquivel, M. Lörgen, N. Sabaté and B. Löchel, *J. Micromech. Microeng.*, 2010, **20**, 115012.
48 S. Tawfick, M. De Volder, D. Copic, S. J. Park, C. R. Oliver, E. S. Polsen, M. J. Roberts and A. J. Hart, *Adv. Mater.*, 2012, **24**, 1628–1674.
49 Y. Mei, S. Kiravittaya, S. Harazim and O. G. Schmidt, *Mater. Sci. Eng., R*, 2010, **70**, 209–224.
50 J.-H. Lee, H. W. Ro, R. Huang, P. Lemaillet, T. A. Germer, C. L. Soles and C. M. Stafford, *Nano Lett.*, 2012, **12**, 5995–5999.
51 K. Yanallah, F. Pontiga and J. Chen, *J. Phys. D: Appl. Phys.*, 2013, **46**, 345202.
52 K. Yanallah and F. Pontiga, *Plasma Sources Sci. Technol.*, 2012, **21**, 045007.
53 D. Chandra, S. Yang and P.-C. Lin, *Appl. Phys. Lett.*, 2007, **91**, 251912.
54 W. T. Huck, N. Bowden, P. Onck, T. Pardoen, J. W. Hutchinson and G. M. Whitesides, *Langmuir*, 2000, **16**, 3497–3501.
55 Y. Yang, X. Han, W. Ding, S. Jiang, Y. Cao and C. Lu, *Langmuir*, 2013, **29**, 7170–7177.
56 W. Ding, Y. Yang, Y. Zhao, S. Jiang, Y. Cao and C. Lu, *Soft Matter*, 2013, **9**, 3720–3726.